To be published in Optics Continuum:

Title:	Backscatter absorption spectroscopy for process monitoring in powder bed fusion
Authors:	Matthias Beuting,Alex Fairhall,Randall Goldsmith,Lianyi Chen,Scott Sanders
Accepted:	18 July 24
Posted	19 July 24
DOI:	https://doi.org/10.1364/OPTCON.529573

Backscatter absorption spectroscopy for process monitoring in powder bed fusion

MATTHIAS BEUTING,[1,*] ALEX J. FAIRHALL,[2] RANDALL H. GOLDSMITH,[2] LIANYI CHEN,[1] SCOTT T. SANDERS,[1]

[1]*Department of Mechanical Engineering, University of Wisconsin-Madison, Madison, WI 53706, USA*
[2]*Department of Chemistry, University of Wisconsin-Madison, Madison, WI 53706 USA*
**matthias.beuting@wisc.edu*

Abstract: Laser powder bed fusion is a metal 3D printing technology that involves melting and solidifying a metal powder using a process laser or electron beam. The interaction of metal vapors with the melt pool is known to cause manufacturing defects. Here we use absorption spectroscopy of laser light reflected from the liquid metal surface to measure atomic Ti vapor during processing of Ti-6Al-4V inside the vapor cavity forming in the melt pool. The absorption line strength and shape were found to vary significantly with processing parameters. In addition, laser-induced fluorescence (LIF) was observed, providing further opportunities for *in situ* diagnostics.

1. Introduction

Powder bed fusion (PBF) is a 3D printing process in which parts are built layer by layer by scanning a focused laser (L-PBF) or electron beam (EB-PBF) over a bed of metal powder. The beam selectively melts the powder fusing it to the previous layers before a new layer of powder is applied and the process is repeated. During melting, the metal partially vaporizes, forming a vapor plume that creates a depression or vapor cavity in the liquid metal as the gas pressure exerts force on the melt pool surface. The vapor cavity, which is steep and narrow under optimal processing conditions in L-PBF, is also referred to as a keyhole which oscillates at a stable frequency due to the complex interplay of gas pressure, metal absorptivity, capillary forces, and liquid metal surface tension [1]. Perturbations to this delicate balance cause instabilities that lead to defects significantly affecting the quality of the parts produced, a concern that has gained urgency as additive manufacturing enters safety-critical industries such as aerospace and medical devices [2,3].

Research has linked melt pool instabilities to a range of issues, including part roughness, porosity, cracks, and mechanical performance [3–5]. Consequently, real-time *in situ* monitoring of melt pool dynamics is crucial for quality control and online parameter adjustment [2,5]. Prior studies have suggested that only a multimodal sensing approach can enhance the fidelity of process monitoring while facilitating a deeper understanding of defect-forming mechanisms [5–7]. A key factor contributing to melt pool instability is the dynamic interaction between the gas in the vapor cavity and the melt pool surface. However, traditional methods for predicting print quality, such as acoustic monitoring and measuring thermal emissions from the melt pool and vapor plume, provide only indirect insights into the gas conditions [4,5].

Here we present a novel approach for process diagnostics in PBF based on laser absorption spectroscopy (LAS) *within* the vapor cavity. This proof-of-principle study investigates the relationship between the absorption signal of atomic Ti and the processing parameters during the processing of a Ti-6Al-4V sample. A sensor derived from this technique could be integrated into existing commercial L-PBF machines for online process monitoring.

2. Backscatter absorption spectroscopy

2.1 Background

The spectral line strength and shape of the elements in the vapor plume depend on the intrinsic and extrinsic conditions of the plume such as its composition, pressure, temperature, and flow velocity. In the past, spectral measurements of the plume have been reported by optical emission spectroscopy (OES), in which the light emitted from the metal vapor plume and the melt pool is collected and analyzed in spectrometers [8,9] or using multiple detectors equipped with spectral filters [10,11]. However, while the OES signal is indicative of plume composition and temperature, it provides only indirect insight into parameters such as pressure and gas velocity. This information is encoded in the shape and precise spectral position of the atomic lines, which typically cannot be resolved by OES.

Recently, absorption spectroscopy has been applied to EB-PBF processes [12,13]. Here, the metal vapor was probed by measuring the absorption of laser light through the vapor plume above the build surface. With tunable laser absorption spectroscopy (TLAS), absorption line shapes can be spectrally resolved allowing by tuning the laser wavelength across an atomic line while measuring the transmission, allowing, e.g., temperature measurements from the Doppler broadening in the near-vacuum conditions in EB-PBF [13]. We have recently demonstrated time-resolved thermometry using TLAS in a single-track EB-PBF experiment targeting a minor alloying element in the metal vapor using a novel vertical cavity surface-emitting laser (VCSEL) [14].

Typically, TLAS requires a line of sight between the light source and a detector [15,16] limiting the studies above to measurements above the vapor cavity. However, efforts have been made to develop single-ended sensors that can detect light reflected or backscattered from rough surfaces even in harsh environments such as combustion chambers and reacting flows [17–20].

We adopt this configuration to measure the absorption within the vapor cavity in powder bed fusion below the metal surface by measuring the light from a probe laser backscattered from the melt pool surface, as shown in Fig. 1. Here, an input probe beam is focused into the vapor cavity and the resulting backscattered TLAS (BTLAS) signal is recorded after passing through the plume twice.

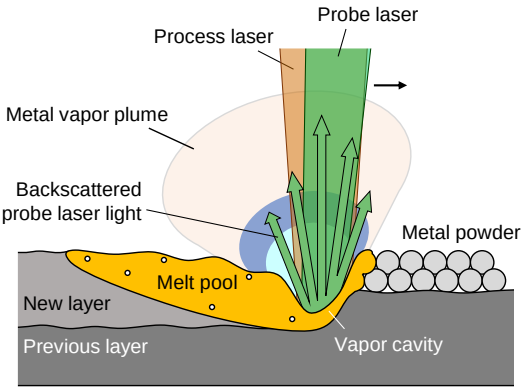

Fig. 1. Backscatter absorption spectroscopy applied to laser powder bed fusion.

2.2 Theory

The attenuation of light traversing through a material is described by Beer's law (1) where I_0 is the initial light intensity, I the intensity after passing through an absorbing medium of thickness L, and S is the line strength. The number density N (particles per unit volume) is proportional to the density, and for an ideal gas, it depends on the gas pressure p, temperature T, and molar

fraction x of the absorber. The (base-e) absorbance A is defined as the negative natural logarithm of the transmission I/I_0.

$$-\ln\left(\frac{I}{I_0}\right) = N(T,p,x)\phi(T,p,\lambda)S(T)L = A(T,p,\lambda,x) \quad (1)$$

Although spectral lines arising from electronic transitions within the atoms have discrete wavelengths λ, the experimentally observed absorption lines exhibit a finite width owing to various line-broadening mechanisms [21]. Their influence is collectively described by the line-shape function ϕ.

While natural broadening, owing to the uncertainty principle, is mostly negligible at elevated temperatures and pressures encountered in laser processing, pressure and Doppler broadening significantly affect the line shape [21]. Pressure broadening results from particle collisions and increases with increasing gas density and temperature, resulting in a Lorentzian line shape. Equation (2) describes its full width at half maximum (FWHM_p), where γ is a broadening coefficient defined at a reference temperature T_{ref} and n is a temperature exponent dependent on the collision partner.

$$\mathrm{FWHM}_p(T,p) = 2\gamma\left(\frac{T_{\mathrm{ref}}}{T}\right)^n p \quad (2)$$

Doppler broadening occurs from the thermal motion of particles, causing spectral lines to undergo a blueshift or redshift, depending on the motion of the particle relative to the observer. This effect leads to a Gaussian line shape, with its full width at half maximum ($\mathrm{FWHM}_{\mathrm{D}}$) described in (3). where M denotes the atomic weight of the absorber.

$$\mathrm{FWHM}_{\mathrm{D}}(T) = 7.16\times10^{-7}\lambda\sqrt{\frac{T}{M}} \quad (3)$$

An additional Doppler shift arising from the gas velocity relative to the propagation of light, distinct from thermal Doppler broadening, can induce a spectral shift in the line center. In backscatter measurements, where light enters the vapor cavity against the bulk flow of expelled gases and exits in the same direction, this results in additional line broadening due to the overlap of the red and blue shifts. The nonrelativistic spectral Doppler shift is given below (4).

$$\lambda_{\mathrm{obs}} = \lambda\sqrt{\frac{1+\frac{v}{c}}{1-\frac{v}{c}}} \quad (4)$$

As illustrated in Fig. 2, the observed absorbance depends on several factors including the number density of the absorber, absorption path length, and gas density or pressure. The resulting line shape function ϕ from Doppler and pressure broadening is a convolution of the Gaussian and Lorentzian profiles, commonly referred to as the Voigt profile [21]. While it is challenging to isolate each of these effects for quantitative measurements, especially in the backscatter configuration where strong gradients may exist, the signal is significantly influenced by gas properties, providing a means for process monitoring or control.

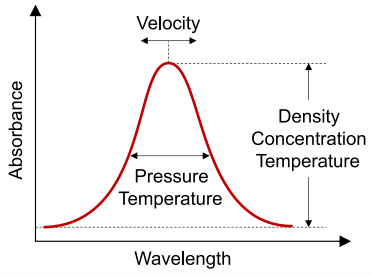

Fig. 2. Effects of gas properties on the spectral profile of atomic transitions under conditions relevant to metal PBF.

3. Experiment

3.1 Laser melting testbed

The testbed shown in Fig. 3a is designed to provide optical access to a stationary melt pool and vapor plume under conditions similar to L-PBF and EB-PBF. It consists of a process laser mounted on top of a vacuum chamber. While the process beam is static, the sample, in the form of a solid Ti-6Al-4V metal disk, is mounted on a rotating and translating motion stage to simulate the motion of the process beam scanning over the powder bed. The chamber is connected to a vacuum roughing pump and an Ar gas cylinder allowing the chamber pressure to be adjusted between 0.1–760 Torr. The vacuum chamber has various ports that can be equipped with optical windows.

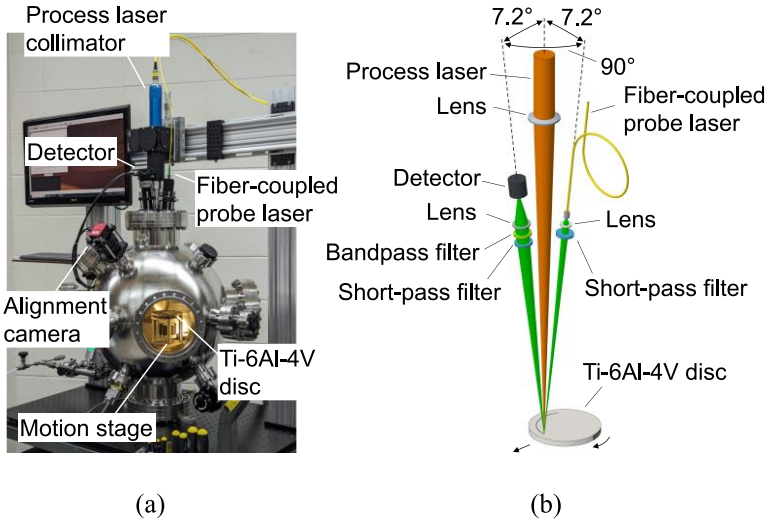

(a) (b)

Fig. 3. (a) The optical testbed and (b) the optical arrangement for the BTLAS approach.

As shown in Fig. 3b, the process laser, a Yb:YAG fiber laser (IPG Photonics YLR, λ_p = 1070 nm, 500 W, beam quality M_q^2 = 5.9; IPG P30 collimator: f = 40 mm, d_0 = 20 mm exit beam diameter), was focused on the sample disk with a focal length f_f = 500 mm lens. The $1/e^2$ spot size calculated using (5) is d_s ~ 200 µm.

$$d_s = \frac{4 f_f \lambda_p M_q^2}{\pi d_0} \tag{5}$$

The top flange of the chamber has viewports that provide optical access nearly coaxial with the process laser, with an offset of ~ 7.2° from the process laser axis. This angle was the smallest achievable considering the space required for the windows and optics on the top flange. One window is used for the probe laser, which is delivered via a single-mode optical fiber (see Section 3.2 for details) and focused on the melt pool using an f = 11 mm aspheric lens with focus adjustment (Thorlabs CFC11A-A), resulting in a spot size of ~ 200 µm similar to the process laser. Adjacent to this is a detector (variable-gain Si photodiode, Thorlabs PDA100A2) that captures the backscattered probe laser light through an f = 40 mm lens. There is a 90° offset between the illumination and detection ports to reduce the amount of specular reflected light reaching the detector and causing intermittent saturation. Both viewports are equipped with fused silica windows with a 30-arcmin wedge to prevent etalon effects caused by interference from light partially reflected within the glass. Short-pass filters (Thorlabs FESH1000, 1000 nm cut-off wavelength) are used to protect the fiber and detector from backscattered process laser light. In front of the detector, a narrow bandpass filter matching the probe laser wavelength (see Section 3.3 for details) further suppresses the process laser light and blocks blackbody radiation

from the melt pool and the vapor plume. With a combined optical density of 13.5 at 1070 nm, both filters effectively suppress the backscattered process laser light. All lenses and windows are anti-reflective coated for the appropriate wavelength. Unless otherwise stated, the optics are made of BK7 glass.

A camera (35 µm/pixel magnification) mounted on one of the 45° ports (Fig. 3a) was used for process monitoring and alignment of the laser beams. To align the beams, the process laser is first used to mark a spot on the metal disk. The probe beam is then adjusted until it aligns with the mark using knobs on a kinematic mount that holds the fiber and optics to the top flange of the vacuum chamber.

3.2 Probe laser

The probe laser used in this experiment was a commercial visible laser configured in a sum frequency generation (SFG) arrangement (M Squared SolsTiS and EMM, 515–661 nm). A narrow-linewidth Ti:sapphire lasing cavity first produces light between 700–1000 nm, which is then coaligned with a 1950-nm fiber laser and mixed inside a periodically-poled lithium niobate (PPLN) crystal. This setup allows for the modulation of the output wavelength over picometers. The generated visible light was coupled into a single mode optical fiber that delivered it to the optical test bed. The optical power at the fiber output was measured to be approximately 10 mW (Thorlabs PM160 power meter). For all absorption measurements in this paper, the tuning bandwidth was set to 20 GHz, corresponding to a tuning range of 18.2 pm at 522 nm. The tuning rate was set to 10 Hz, i.e., the frequency at which the wavelength is modulated from the lowest to the highest wavelength and back (Fig. 4).

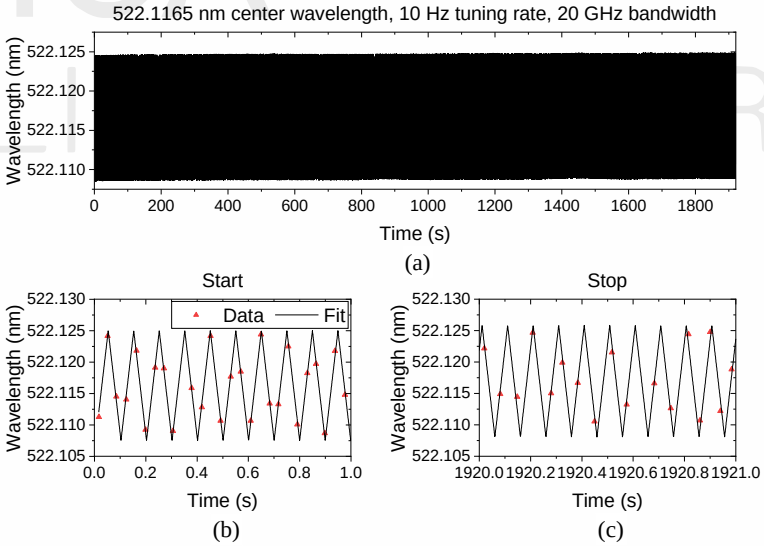

Fig. 4. Long-term spectral measurement characterizing the laser scanning method. The full trace (a) shows the overall stability and consistency despite undersampling, as demonstrated by cuts in the scan starting (b) and stopping (c) periods.

To evaluate the wavelength tuning stability, the output of the laser system was monitored with wavemeter (HighFinesse WS6-600, 600 MHz accuracy) over a time span of 30 min while the laser was tuned (Fig. 4). Since the sampling rate of the wavemeter was limited to 25 Hz, the tuning rate and range were determined by fitting a symmetrical sawtooth function to the under-sampled data for small time windows of 10 wavelength sweeps each, as shown in Figs. 4a and 4b. The resulting tuning rate from the individual fits averaged 10.000 Hz over the whole dataset with a standard deviation of 0.0016 Hz, while the tuning range was 17.3 pm with a standard

deviation of 0.32 pm, slightly less than the target tuning range. However, the tuning rate was also observed to vary between measurement days. Since the experimental setup did not allow simultaneous monitoring of the laser wavelength with the wavemeter during the experiments, we decided not to derive a wavelength axis from the time trace. Consequently, all signals in Section 4 are presented as a function of time instead of wavelength.

It is important to note that the probe laser power is more than four orders of magnitude lower than the process laser powers used in this work, so the influence of the probe beam on the melt pool is negligible.

3.3 Line selection

Using the gas temperature reported in previous studies [13,14], spectral simulations were performed (Fig. 5) to identify candidate Ti absorption lines within the spectral range accessible by the probe laser (see [14] for details on the simulations). Since pressure, absorption path length, and Ti concentration are largely unknown at this point and were therefore arbitrarily chosen for the simulations, the optical bandpass (Thorlabs FBH520-10, 520 nm central wavelength, 10 nm bandwidth) was chosen to accommodate multiple Ti lines with significantly different absorption (dashed green line in Fig. 5).

Initial tests (not shown) showed that the absorption of the stronger lines was too strong, causing the plume to be completely opaque. Therefore, the weakest line within this range at 522.155 nm ($3d^2 4s^2$ a ^{3}F 3 → $3d^2(^3F)4s4p(^3P°)$ z ^{3}F° 2 [22], red arrow in Fig. 5) was selected for all absorption measurements.

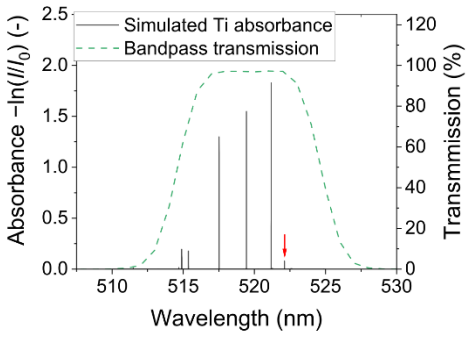

Fig. 5. Simulation of Ti absorption assuming a temperature of 3000 K at quasi-vacuum pressure for an absorption path length of 200 µm (see [14] for details) along with the bandpass transmission curve. The red arrow marks the line selected for the experiments presented in Section 4 unless stated otherwise.

4. Results

For each measurement sequence, the Ti-6Al-4V disk was accelerated to reach the desired speed (400 mm/s unless stated otherwise) at the process beam location. The process laser was then activated for the full rotation of the sample disk. During the entire run-up and measurement sequence, the probe laser was active and tuned over the target absorption line, while data acquisition (National Instruments PXIe-1062Q and PXI-5105) was triggered just before the process laser was activated. The hatch distance between two consecutive scans was 0.2 mm.

Figure 6 shows the raw signal recorded during a measurement sequence. As soon as the process laser is triggered, the signal level increases significantly. This is consistent with the backscattered light becoming more directional: as the vapor cavity forms, the beam angle is expected to become smaller because the light escapes mainly upward through the aperture after multiple reflections from the walls of the vapor cavity [23]. As a result, more light reaches the nearly coaxial detector.

The intensity and shape of the recorded signal has been found to depend significantly on the process parameters applied to the signal, as described in the following sections.

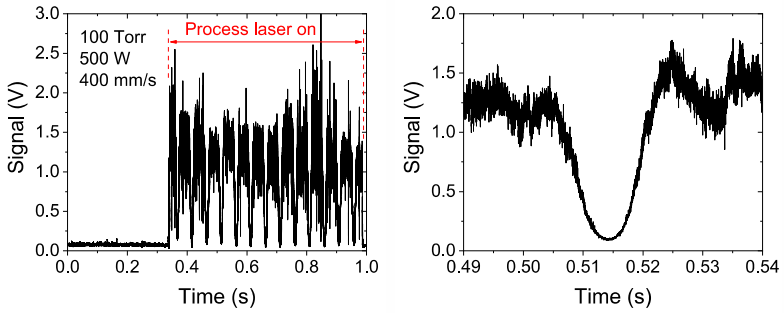

Fig. 6. (a) the raw signal versus time curve recorded at a laser power of 500 W at a scan speed of 400 mm/s in a 100-torr Ar atmosphere and (b) the same curve zoomed in on a single wavelength sweep of the probe laser across the Ti spectral line.

4.1 Signal intensity

The intensity of the backscattered signal depends on the attenuation of the probe laser light due to absorption at the melt surface and the angle at which it is reflected depending on the shape of the vapor cavity, which depends on the processing parameters. During the experiments, the process laser power and the test chamber Ar pressure were varied. Figure 7 shows the signal ensemble-averaged over six scans for different process laser powers (a) and pressures (b). Here, the *x*-axis represents the time relative to the time at which the peak absorbance of each of the six scans is observed.

The probe laser signal level increases with process laser power at a constant pressure of 100 Torr. This can be explained by the increasing depth of the vapor cavity with increasing laser power, resulting in more directed backscatter [23], and, therefore, more light reaching the detector.

With increasing pressure, however, first an increase of the signal level between 0.1–100 Torr can be observed before it drops between 100–700 Torr. This is consistent with the simulations by Li et al. [24] who observed a shallow and round vapor cavity at 10 mbar as the vapor jet is expelled at a large divergence angle in the low-pressure environment. With increasing chamber pressure, their simulations show that the vapor cavity becomes initially steeper and deeper before it becomes shallower again at significantly higher pressure. This could be caused by the reduced recoil pressure as the pressure difference between the vapor cavity pressure and the chamber pressure decreases.

Another explanation for the drop at higher pressure could be plasma shielding from partial ionization of the metal vapor, since the temperature in the vapor cavity increases with chamber pressure due to the higher boiling point of the metals at elevated pressure. However, as pointed out by Hanemann et al. [25], the laser fluence in L-PBF is probably insufficient for ionizing the gases in the plume. We calculated the ionization fraction using the Saha equation [26] (not shown) to be on the order of 0.1% near the boiling point of Ti (3558 K) at ambient pressure. Although the ionization fraction is small, it could have some influence on the delicate balance of forces in the vapor cavity. However, we did not observe any optical emission from ionized Ti during this study (see Fig. 12 for emission spectra) and never observed any ion emission during initial testing of the optical testbed when measuring the emission between 300–500 nm with a high-resolution spectrometer (not shown) at near vacuum pressure. However, while the ionization fraction increases with temperature, it also decreases with pressure. Therefore, there

may be conditions in the pressure and temperature range in L-PBF where the influence of plasma shielding is relevant.

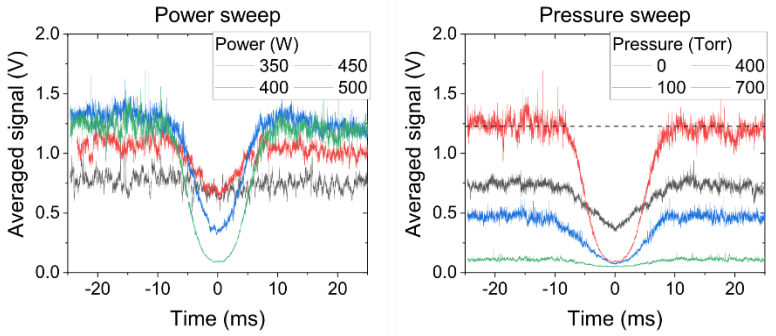

Fig. 7. BTLAS signal at 400 mm/s scan speed for varying process laser power at 100 Torr (a) and test chamber pressure at 500 W (b). The plots shown were averaged over six consecutive laser sweeps to reduce noise.

4.2 Absorbance

The absorbance is calculated using (1) using the averaged signal (Fig. 7) as I, whereas I_0 is determined by fitting a horizontal baseline to the data trace (dashed line in Fig. 7b). This baseline correction makes the calculation of the absorbance independent of the overall signal intensity. As shown in Fig. 8a, the absorbance increases with increasing laser power. This trend is consistent with previous findings, where mass loss rates increased with the process beam power [27]. For the pressure sweep (Fig. 8b), the absorbance first increases with pressure before it decreases again. [24]

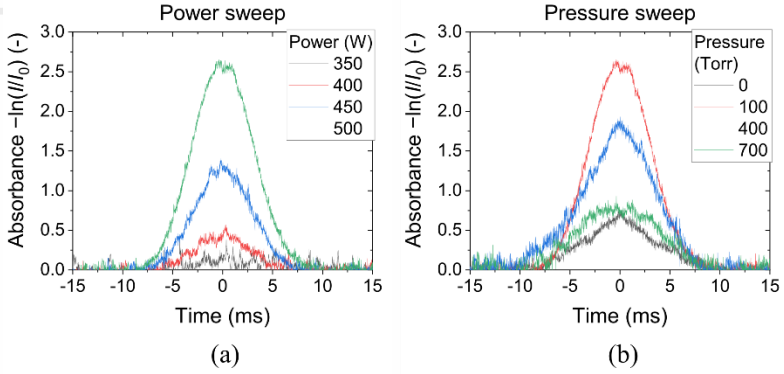

Fig. 8. Absorbance derived from the intensity data in Fig. 7 showing a significant dependence on (a) the process laser power at a constant chamber pressure of 100 Torr and (b) chamber pressure at a constant process laser power of 500 W, both at a scan speed of 400 mm/s.

We hypothesize that two competing effects explain this behavior:

(a) Increasing pressure increases the boiling point which reduces the mass loss rate (i.e., the amount of vaporized material) [28] leading to reduced absorption due to a lower absorber number density. Figure 9 shows the boiling point of Ti as a function of the pressure calculated using data from Ref. [29]. The boiling point increases rapidly from 2205–3123 K between 0.1–100 Torr before approaching an asymptote at higher pressure.

(b) Increasing pressure linearly increases the total gas number density, assuming an ideal gas, resulting in increased absorption.

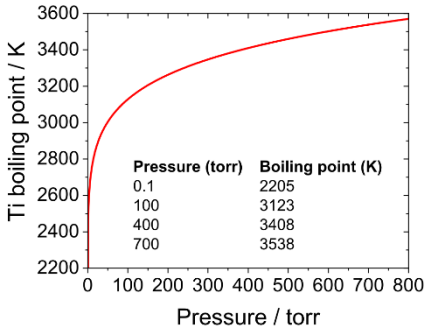

Fig. 9: Boiling point of Ti calculated using the Clausius-Clapeyron equation referencing the boiling point (3558 K) at ambient pressure (760 Torr) [29].

The boiling point increase is logarithmic with pressure whereas the density increase is linear with pressure, making a pronounced minimum in measured absorbance plausible. However, the boiling point of Ti6Al4V (3315 K at ambient conditions) differs significantly from that of pure Ti and modeling the mass loss rate as a function of the melt pool temperature is not trivial [28]. Therefore, further studies are needed to confirm that the two mechanisms described above are responsible for the observations.

4.3 Line shape

Variations in line shape are evident when examining the normalized absorbance (Fig. 10). During the power sweep at 100 Torr (Fig. 10a), the line shape remained invariant, suggesting that the gas temperature remains constant, indicating that evaporation takes place under equilibrium conditions [13].

During the pressure variation (Fig. 10b), the Ti line width initially narrows with increasing pressure up to 100 Torr and then broadens again to 700 Torr. This behavior is attributed to the interplay of line-broadening effects: The broadening between 100–700 Torr is consistent with the increased pressure broadening due to the increased chamber pressure. Additionally, increased Doppler broadening occurs due to the rising plume temperature because of the increased boiling point at higher pressures.

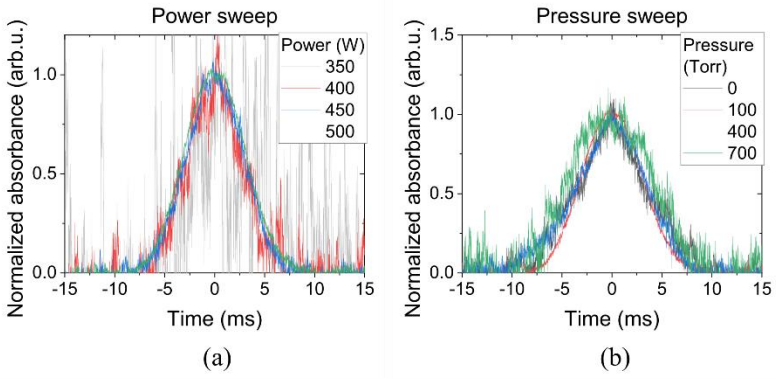

Fig. 10. Normalized absorbance during (a) the process laser power sweep at 100 Torr and (b) the pressure sweep at 500 W at a scan speed of 400 mm/s showing differences in line shape depending on the process parameters.

The initial narrowing between 0 and 100 Torr can be attributed to Doppler shifts (not to be confused with Doppler broadening) because of the increased velocity at which the gas is expelled from the vapor cavity in vacuum: As the probe beam passes through the vapor, first against and then in the direction of flow, the signal undergoes a redshift and a blueshift, respectively. Using the gas velocity of 1500 m/s observed by Li et al. [24] at 10 mbar, the resulting Doppler shift was approximately 2.6 pm (4), which is similar in magnitude to the expected linewidth in vacuum [14]. Since the gas velocity decreases with chamber pressure, the influence of this effect would explain an apparent line narrowing over the 0–100 Torr range.

The observed line shapes were found to be near-Gaussian at all investigated conditions as shown in Fig. 11. At low pressure, it has been shown that Doppler broadening is the only dominant broadening mechanism [13] explaining the Gaussian shape at 0.1 Torr. This might also be the case for the higher-pressure cases, since pressure broadening would lead to a more Lorentzian line shape. Without wavelength calibration and without published broadening coefficients for Ti-Ti and Ti-Ar collisional broadening, we cannot distinguish between self-broadening (resonance broadening) and the influence of the bath gas on the line width at this point.

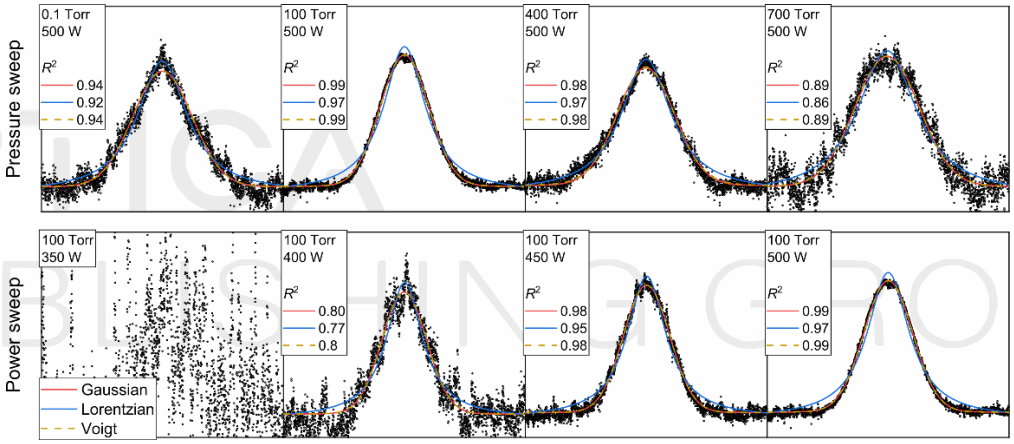

Fig. 11: Line shapes measured during the pressure and power sweep with Gaussian, Lorentzian, and Voigt line shape fits (wherever the fit converged) and corresponding coefficients of determination R^2. The Gaussian fits generally approximate the line shapes better with also the Voigt fit converging to a Gaussian line shape.

It is important to emphasize that the analysis presented in this section is largely qualitative, with some speculative elements. To fully discern the interplay of mechanisms affecting line shape and strength, alternative or supplementary measurements and a more comprehensive understanding of the dynamics between gases in the vapor cavity and the melt pool are needed. Nevertheless, the pronounced variability in the observed signals based on processing parameters highlights the potential for advanced process monitoring and closed-loop control, potentially leveraging techniques such as machine learning.

4.4 Laser-induced fluorescence

The optical emission from the plume was also measured by replacing the detector with an optical fiber (Ocean Optics XSR, 450 µm, 180–800 nm) delivering light to a spectrometer (Optosky ATP2000P, 2.1 nm resolution, 2 ms exposure time). The bandpass filter on the detection side was replaced with a neutral density filter (Thorlabs ND10) to capture light in the visible range without overexposing the spectrometer.

Figure 12 shows the plume emission spectrum both without the probe laser and with the probe laser tuned to the stronger 519.442 nm line shown in Fig. 5. In the absence of the probe laser (black curve), no emission lines were visible. However, when the probe laser was on (red

curve), Ti lines became clearly visible, suggesting that these lines are due to laser-induced fluorescence (LIF), which is the spontaneous emission of light upon stimulated excitation by absorption of laser light.

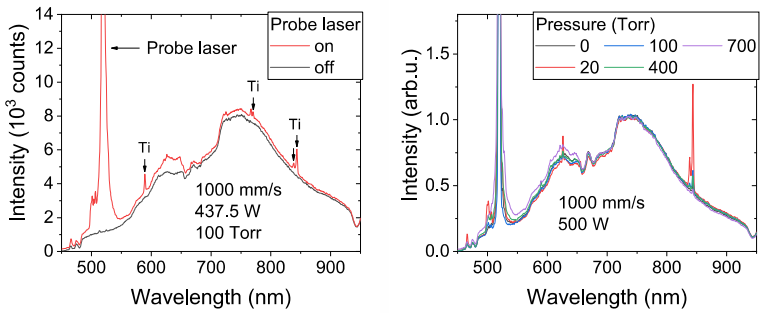

Fig. 12. (a) Emission spectrum without probe laser and with probe laser tuned to the stronger 519.4415-nm absorption line showing laser-induced fluorescence (LIF) and (b) LIF signal for varying chamber pressures at a scan speed of 1000 mm/s.

While there is likely some non-stimulated emission from hot Ti, it is not detectable with the low-resolution spectrometer used in our study. This instrument under-resolves atomic lines by about three orders of magnitude, causing the low-resolution lines to blend into the background signal and become undetectable.

The fluorescence signal varied significantly with chamber pressure, peaking at 20 Torr. This correlates with the observations from the absorbance measurements, where the signal level and absorbance are the highest, while the line width is the lowest at intermediate and low pressures.

5. Discussion

5.1 Speckle noise

The relatively high noise level scales with the signal intensity, indicating that it is caused by speckle noise, which is expected and largely unavoidable. When coherent light is reflected from rough surfaces, speckle patterns, as shown in Fig. 13a, can be observed owing to the interference of the laser light scattered from the high and low points of the rough surface of the illuminated area. The interference pattern changes with the surface speckle, thus changing the signal reaching the detector and resulting in transient noise.

Figure 13b shows the Fourier transform power spectrum of the backscattered signal for the stationary sample disk, the moving sample disk, and during an absorption measurement. When comparing the power spectra of the stationary disk with the moving disk, it becomes evident that the noise caused by motion extends to about 6 kHz. This is similar in magnitude to the speckle noise frequency of 2.5–25 kHz observed by Wang and Sanders [19] from a rough surface moving at 300–3000 mm/s. The noise recorded during the absorption measurement extends beyond the measurement range though also dropping at 6 kHz. This is consistent with recent research suggesting that keyhole oscillations occur at 40 kHz or faster [30], with the surface significantly changing several times during each oscillation cycle.

To reduce the influence of speckle noise, the laser must be tuned faster than the rate at which the surface of the melt pool changes. Here, increasing the tuning rate to values well above 6 kHz largely will eliminate the influence of the sample disk motion. To further reduce the influence of melt pool oscillations, the required tuning rate is likely to be in the range of hundreds of kilohertz. Such rates have been routinely achieved using, for example, diode lasers [31,32].

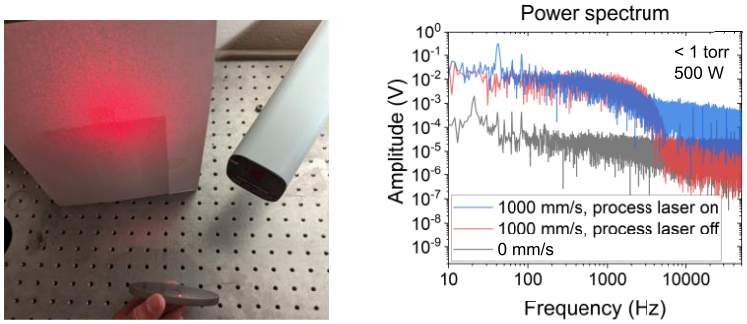

(a) (b)

Fig. 13. (a) Speckle pattern generated by HeNe laser beam scattered off the sample disk surface; (b) Power spectrum obtained through Fourier transformation of the measured signal, comparing a stationary disk to a spinning sample disk, both with and without the process laser.

Transient speckle noise can also result from tuning the wavelength of the probe beam. Assuming a typical root mean square (rms) roughness for the powder bed PBF of h_{rms} = 20 µm (Ti-6Al-4V, D50 = 32 µm) [33], the wavelength change needed to alter the speckle pattern is $\Delta\lambda$ = ~ 1.5 nm (6) [19]. Since the probe laser tuning range needed for atomic line measurements is about 2 orders of magnitude lower (16 pm in this work, see Section 3.2), speckle noise originating from wavelength tuning can be neglected.

$$\Delta\lambda = \frac{\lambda^2}{\lambda + 2\sqrt{2}\pi h_{rms}} \tag{6}$$

5.2 Representativeness

The conditions of the metal vapor in this simplified experiment differ from the still largely unknown conditions in the vapor cavity in L-PBF. The main differences are the larger spot size and slower scan speed compared to most production machines, use of a solid sample instead of metal powder, and the absence of a shielding gas flow. Further work is required to determine whether the technique is applicable to real-world conditions (see Section 6).

Furthermore, spatter and ejected powder could be additional sources of scattered light in the L-PBF process. Moreover, the absorption of light by droplets and nanoparticles of condensing metal vapor could be wavelength dependent due to size effects if the particle size is similar to the wavelength of the interrogation laser light. However, these sources of scattered light above the vapor cavity are to some extent out of focus, so that light collection is less efficient, reducing their influence on the overall signal. Further research on the influence of gas-borne particles is needed when applying the BTLAS technique to L-PBF.

6. Conclusions and path forward

The feasibility of backscatter absorption spectroscopy of gases within the vapor cavity produced during laser processing of solid Ti-6Al-4V was demonstrated. The signal stemming from atomic Ti lines varies significantly with the laser power and build chamber pressure, indicating its potential in process monitoring for quality monitoring or closed-loop feedback control of processing parameters in 3D printing.

For a practical impact, the technique should be integrated into existing machines and the time resolution should be increased to capture the dynamics of the melt pool/vapor plume interactions. In addition, attempts to mitigate the effects of speckle noise should be pursued.

Application to PBF

Before applying the BTLAS technique to production machines, a reasonable next step could be its application to L-PBF or EB-PBF in single-track experiments with metal powders under

realistic conditions. For this purpose, the probe beam can be fixed in space while the process beam is scanned across the probe beam spot, similar to previous work studying the metal vapor plume with absorption spectroscopy [12–14]. Here, the ability of single-track testbeds to apply complementary measurement techniques such as X-ray imaging [34,35] can be leveraged to test if and how the BTLAS signal correlates with defects such as pore formation.

Machine integration

Coaxial integration is an obvious solution to equip production L-PBF machines with BTLAS sensors. To this end, a dichroic mirror can be used to combine the probe and process laser. The backscattered light could either be detected by a sensor inside the build chamber or even though the same optical path as the laser beams.

Multi-line measurements

Employing multiple probe beams concurrently can facilitate the targeting of absorption lines from different alloying elements. Signal ratios would then offer insights into the individual mass loss rates of each species. Furthermore, targeting absorption lines with variable temperature dependence could allow quantitative temperature measurements.

Laser-induced fluorescence

It should be further explored whether laser-induced fluorescence has potential as a diagnostic tool in additive manufacturing. While high-energy pulsed lasers have been successfully used for LIF experiments in laser welding [36–38], this work showed that relatively low-powered CW lasers can also be used to significantly boost the emission of the vapor plume compared with optical emission spectroscopy of thermally excited metal vapor.

Fundamental research

Attention should be paid to determining whether the gas in the vapor cavity comprises neutral atoms or plasma. We did not detect any ionized species in this study. Nonetheless, it remains uncertain whether the observed signal decrease at elevated process laser powers and pressures can be attributed to plasma shielding.

Funding. U.S. Department of Commerce (grant number 70NANB21H039); National Institute of Health (grant number GM-136981); National Defense Science and Engineering Graduate Fellowship Program, sponsored by the Air Force Research Laboratory, the Office of Naval Research, and the Army Research Office (FA9550-21-F-0003).

Disclosures. A patent application covering the technology described in this manuscript has been filed and is currently pending (application number U.S. 18/231066). There are no other competing interests.

Data availability. Data underlying the results presented in this paper are available on *Zenodo* under DOI: 10.5281/zenodo.10602517.

References

1. N. Kouraytem, X. Li, R. Cunningham, C. Zhao, N. Parab, T. Sun, A. D. Rollett, A. D. Spear, and W. Tan, "Effect of Laser-Matter Interaction on Molten Pool Flow and Keyhole Dynamics," Phys Rev Appl **11**, 064054 (2019).
2. P. Yadav, O. Rigo, C. Arvieu, E. Le Guen, and E. Lacoste, "In Situ Monitoring Systems of The SLM Process: On the Need to Develop Machine Learning Models for Data Processing," Crystals (Basel) **10**, 524 (2020).
3. M. Wegner, T. S. Hartwich, E. Heyden, L. Schwan, J. Schwenke, N. Wortmann, and D. Krause, "New Trends in Aviation and Medical Technology Enabled by Additive Manufacturing," Front Manuf Technol **2**, (2022).
4. D. Wang, H. Han, B. Sa, K. Li, J. Yan, J. Zhang, J. Liu, Z. He, N. Wang, and M. Yan, "A review and a statistical analysis of porosity in metals additively manufactured by laser powder bed fusion," Opto Electron Adv **5**, 210058–210058 (2022).
5. M. Grasso, A. Remani, A. Dickins, B. M. Colosimo, and R. K. Leach, "In-situ measurement and monitoring methods for metal powder bed fusion: an updated review," Meas Sci Technol **32**, 112001 (2021).

6. J. Liu, B. Wei, H. Chang, J. Li, and G. Yang, "Review of Visual Measurement Methods for Metal Vaporization Processes in Laser Powder Bed Fusion," Micromachines (Basel) **14**, 1351 (2023).
7. A. A. Martin, N. P. Calta, S. A. Khairallah, J. Wang, P. J. Depond, A. Y. Fong, V. Thampy, G. M. Guss, A. M. Kiss, K. H. Stone, C. J. Tassone, J. Nelson Weker, M. F. Toney, T. van Buuren, and M. J. Matthews, "Dynamics of pore formation during laser powder bed fusion additive manufacturing," Nat Commun **10**, 1987 (2019).
8. C. S. Lough, L. I. Escano, M. Qu, C. C. Smith, R. G. Landers, D. A. Bristow, L. Chen, and E. C. Kinzel, "In-situ optical emission spectroscopy of selective laser melting," J Manuf Process **53**, (2020).
9. A. R. Ziefuss, R. Streubel, P. Gabriel, F. Eibl, and S. Barcikowski, "In-situ monitoring of the material composition in PBF-LB via optical emission spectroscopy," ChemRxiv. This content is a preprint and has not been peer-reviewed. (2023).
10. A. J. Dunbar and A. R. Nassar, "Assessment of optical emission analysis for in-process monitoring of powder bed fusion additive manufacturing," Virtual Phys Prototyp **13**, 14–19 (2018).
11. M. Montazeri, R. Yavari, P. Rao, and P. Boulware, "In-Process Monitoring of Material Cross-Contamination Defects in Laser Powder Bed Fusion," J Manuf Sci Eng **140**, (2018).
12. A. el Farsy, E. C. Tighidet, C. Ballage, and T. Minea, "Spatiotemporal characterization of evaporated atoms during electron beam melting additive manufacturing by advanced laser diagnostics," J Appl Phys **133**, 044901 (2023).
13. A. el Farsy, V. G. Antunes, B. Seznec, L. Schiesko, C. Ballage, and T. Minea, "Saturation pressure of nonequilibrium titanium evaporation during additive manufacturing by electron powder bed fusion," J Appl Phys **132**, 054904 (2022).
14. M. Beuting, L. I. Escano, L. Chen, and S. T. Sanders, "Time-resolved absorption spectroscopy in electron beam melting with blue vertical-cavity surface-emitting lasers," Opt Express **31**, 17268 (2023).
15. C. S. Goldenstein, R. M. Spearrin, Jay. B. Jeffries, and R. K. Hanson, "Infrared laser-absorption sensing for combustion gases," Prog Energy Combust Sci **60**, 132–176 (2017).
16. C. Liu and L. Xu, "Laser absorption spectroscopy for combustion diagnosis in reactive flows: A review," Appl Spectrosc Rev **54**, 1–44 (2019).
17. S. T. Melin, Z. Wang, N. J. Neal, D. A. Rothamer, and S. T. Sanders, "Single-ended retroreflection sensors for absorption spectroscopy in high-temperature environments," Appl Phys B **123**, 119 (2017).
18. W. Y. Peng, C. S. Goldenstein, R. Mitchell Spearrin, J. B. Jeffries, and R. K. Hanson, "Single-ended mid-infrared laser-absorption sensor for simultaneous in situ measurements of H_2O, CO_2, CO, and temperature in combustion flows," Appl Opt **55**, 9347 (2016).
19. Z. Wang and S. T. Sanders, "Toward single-ended absorption spectroscopy probes based on backscattering from rough surfaces: H_2O vapor measurements near 1350 nm," Appl Phys B **121**, 187–192 (2015).
20. Y. Zhou, G. C. Mathews, and C. S. Goldenstein, "Compact, fiber-coupled, single-ended laser-absorption-spectroscopy sensors for high-temperature environments," Appl Opt **57**, 7117 (2018).
21. A. C. Eckbreth, *Laser Diagnostics for Combustion Temperature and Species*, 2nd ed. (Taylor & Francis, 1996), Vol. 3.
22. A. Kramida, Yu. Ralchenko, J. Reader, and NIST ASD Team, "NIST Atomic Spectra Database (version 5.9)," https://physics.nist.gov/asd.
23. B. Lane, I. Zhirnov, S. Mekhontsev, S. Grantham, R. Ricker, S. Rauniyar, and K. Chou, "Transient Laser Energy Absorption, Co-axial Melt Pool Monitoring, and Relationship to Melt Pool Morphology," Addit Manuf **36**, 101504 (2020).
24. X. Li, Q. Guo, L. Chen, and W. Tan, "Quantitative investigation of gas flow, powder-gas interaction, and powder behavior under different ambient pressure levels in laser powder bed fusion," Int J Mach Tools Manuf **170**, (2021).
25. T. Hanemann, C. Seyfert, P. Holfelder, A. Rota, and M. Heilmaier, "Dimensionless Enthalpy as Characteristic Factor for Process Control in Laser Powder Bed Fusion," Journal of Laser Micro/Nanoengineering **15**, 257–266 (2020).
26. A. Fridman, *Plasma Chemistry* (2008).
27. D. Deisenroth, S. Mekhontsev, and B. Lane, "Measurement of mass loss, absorbed energy, and time-resolved reflected power for laser powder bed fusion," in *Laser 3D Manufacturing VII*, H. Helvajian, B. Gu, and H. Chen, eds. (SPIE, 2020), p. 20.
28. L. Wang, Y. Zhang, and W. Yan, "Evaporation Model for Keyhole Dynamics During Additive Manufacturing of Metal," Phys Rev Appl **14**, 064039 (2020).
29. W. F. Gale and T. C. Totemeier, *Smithells Metals Reference Book* (Elsevier, 2003).
30. Z. Ren, L. Gao, S. J. Clark, K. Fezzaa, P. Shevchenko, A. Choi, W. Everhart, A. D. Rollett, L. Chen, and T. Sun, "Machine learning–aided real-time detection of keyhole pore generation in laser powder bed fusion," Science (1979) **379**, 89–94 (2023).
31. A. Farooq, A. B. S. Alquaity, M. Raza, E. F. Nasir, S. Yao, and W. Ren, "Laser sensors for energy systems and process industries: Perspectives and directions," Prog Energy Combust Sci **91**, (2022).
32. A. P. Nair, N. Q. Minesi, C. Jelloian, N. M. Kuenning, and R. M. Spearrin, "Extended tuning of distributed-feedback lasers in a bias-tee circuit via waveform optimization for MHz-rate absorption spectroscopy," Meas Sci Technol **33**, 105104 (2022).

33. K. Yuasa, M. Tagami, M. Yonehara, T.-T. Ikeshoji, K. Takeshita, H. Aoki, and H. Kyogoku, "Influences of powder characteristics and recoating conditions on surface morphology of powder bed in metal additive manufacturing," The International Journal of Advanced Manufacturing Technology **115**, 3919–3932 (2021).
34. C. Zhao, K. Fezzaa, R. W. Cunningham, H. Wen, F. De Carlo, L. Chen, A. D. Rollett, and T. Sun, "Real-time monitoring of laser powder bed fusion process using high-speed X-ray imaging and diffraction," Sci Rep **7**, 3602 (2017).
35. C. Ioannidou, H.-H. König, N. Semjatov, U. Ackelid, P. Staron, C. Körner, P. Hedström, and G. Lindwall, "In-situ synchrotron X-ray analysis of metal Additive Manufacturing: Current state, opportunities and challenges," Mater Des **219**, 110790 (2022).
36. B. J. Simonds, P. Williams, and J. Lehman, "Time-resolved detection of vaporization during laser metal processing with laser-induced fluorescence," Procedia CIRP **74**, (2018).
37. B. J. Simonds, B. Tran, and P. A. Williams, "In situ monitoring of Cu/Al laser welding using Laser Induced Fluorescence," Procedia CIRP **94**, (2020).
38. B. J. Simonds, J. W. Sowards, and P. A. Williams, "Laser-induced fluorescence applied to laser welding of austenitic stainless steel for dilute alloying element detection," J Phys D Appl Phys **50**, (2017).